

# Final Report: Seismic Velocity Structure of Harrat Lunayyir, northwestern Saudi Arabia

## Principal Investigators (PIs):

Samantha E. Hansen, Dept. of Geological Sciences, University of Alabama

Abdullah M.S. Al-Amri, Seismic Studies Center, King Saud University

## Overview

In 2009, a swarm of more than 30,000 earthquakes occurred beneath the Harrat Lunayyir lava field in northwest Saudi Arabia. Surface deformation associated with the seismicity, modeled in previous studies using Interferometric Synthetic Aperture Radar (InSAR) data, is best attributed to the intrusion of a 10-km-long dyke (Baer and Hamiel, 2010; Pallister et al., 2010). However, little is known about the velocity structure beneath Harrat Lunayyir, making assessment of future seismic and volcanic hazards difficult. We have used local double-difference tomography to generate a P-wave velocity model beneath Harrat Lunayyir and to more precisely locate earthquakes from the 2009 seismic swarm. This final report summarizes our findings, which were published in *The Journal of Geophysical Research* (Hansen et al., 2013).

## Seismic Data

When seismic activity began in April 2009, the Harrat Lunayyir region was instrumented with 29 seismometers operated by the Saudi Geological Survey (SGS), the King Abdulaziz City of Science and Technology (KACST), and King Saud University (KSU; Fig. 1). Given the limited availability of broadband SGS data, most of our analysis is based on data from the 16 KACST and KSU stations, which were equipped with short-period, one component (vertical) SS-1 Ranger seismometers with sampling rates of 100 sps. Data for 5710 earthquakes, occurring between April 30 and July 31, 2009, were provided for analysis (Fig. 1). Since the full dataset was not obtained until February 25, 2012, a no-cost extension was granted for the project, extending funding until June 1, 2013.

Given the large quantity of data produced by the seismic swarm, it was not feasible to hand-pick all of the Harrat Lunayyir seismograms. Instead, we employed the Akaike Information Criteria (AIC) phase picker developed by Zhang et al. (2003). This automatic P-wave arrival detection and picking algorithm applies a wavelet transformation through a series of sliding time windows. In each window, the autopicker is applied to the absolute wavelet coefficient. If the picks are consistent at three different scales, the phase arrival is marked within that time window (Fig. 2; Zhang et al., 2003). The AIC picker needs a starting reference point, so initial P-wave picks were made using *taup\_setsac* (Crotwell and Owens, 1998) and the ak135 Earth model (Kennett et al., 1995).

The bispectrum cross-correlation package for seismic events (BCSEIS; Du et al., 2004) was also used to determine cross-correlation (CC) coefficients and to compute high-precision differential travel-times between event pairs recorded at the same station. Differential times computed by

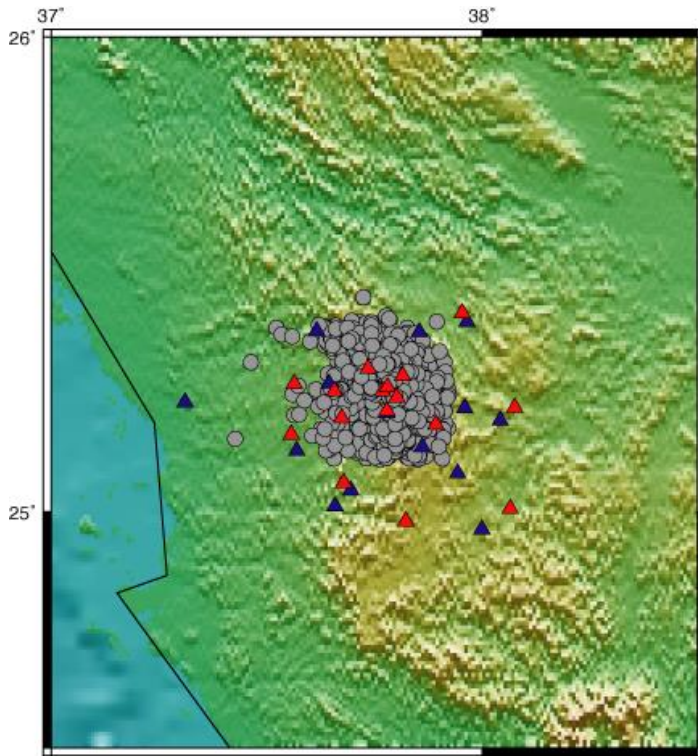
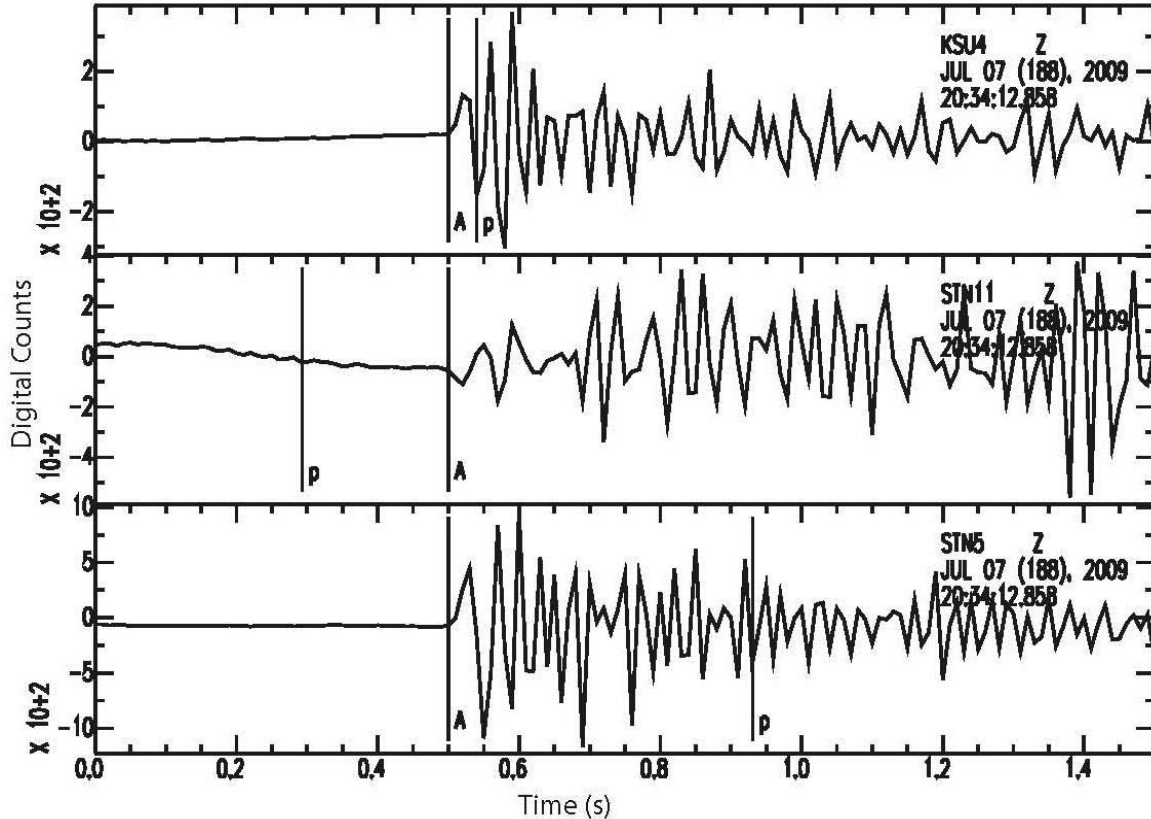


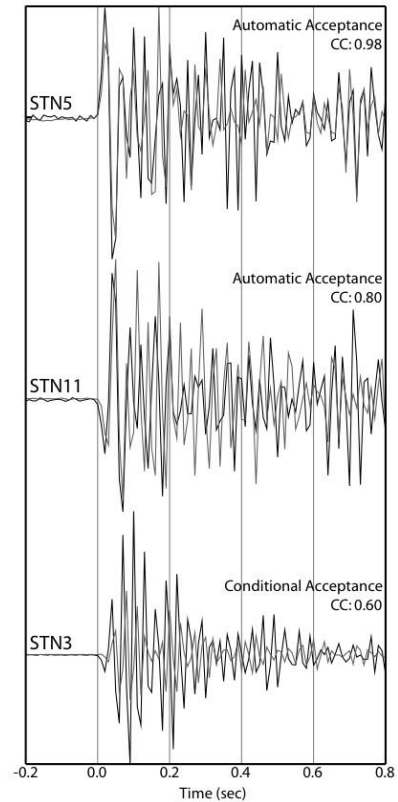
**Figure 1.** KACST-KSU and SGS stations are shown by red and blue triangles, respectively. Initial earthquake locations are shown by the gray dots. Background topography is from the 30 s digital elevation map in GMT (Wessel and Smith, 1998).

**Figure 2.** Examples of P-waves picked by the AIC picker. The three panels show the vertical component seismogram from three different Harrat Lunayyir stations (KSU4, STN11, and STN5) for a magnitude 0.1 event that occurred on July 7, 2009. Vertical lines denoted with “p” are the predicted P-wave arrival times determined by *taup\_setsac* (Crotwell and Owens, 1998) using the *ak135* reference model (Kennett et al., 1995). Lines denoted with “A” are the P-wave picks made by the AIC picker.



this method can be used with the double-difference family of earthquake location and tomography algorithms (such as *tomoDD*). Including such measurements can help to improve event relocation results. Differential times from event pairs with correlation coefficients  $\geq 0.75$  were automatically accepted for use in later analysis. BCSEIS also permits event pairs with lower coefficients to be retained if they meet user-specified criteria (Du et al., 2004). For our analysis, event pairs with coefficients  $\geq 0.50$  were also accepted if at least one other station for the event pair has a coefficient  $\geq 0.90$  (Fig. 3). This is useful for stations that have a low signal-to-noise ratio or particular site effects.

**Figure 3.** Examples of cross-correlated waveforms identified by BCSEIS (Du et al., 2004). Event 1 (black waveforms) occurred on May 23, 2009, and event 2 (gray waveforms) occurred on May 30, 2009. Stations STN5 and STN11 both have CC coefficients  $\geq 0.75$ , so the corresponding differential travel-times are automatically accepted. Station STN3 has a lower CC coefficient, but because the CC coefficient is at least 0.90 at another station, the differential travel-time for station STN3 is also accepted.



### 1D Minimum Starting Model

The results of tomographic inversion are dependent on the starting reference model and the quality of the initial hypocenter locations (Michael, 1988; van der Hilst and Spakman, 1989; van der Hilst et al., 1991). Many tomographic studies begin with a simple, smoothed model utilized in a 1D inversion. The resulting 1D model can then be used as a reference model for a 3D tomographic study. Using the approach outlined by Kissling et al. (1994), the VELEST program was used to determine a minimum 1D model for the Harrat Lunayyir region.

An *a priori* 1D model was first developed based on a collection of past studies in the Arabian Shield, including receiver functions, group velocities, and seismic refraction (Mooney et al., 1985; Sandvol et al., 1998; Rodgers et al., 1999; Julia et al., 2003; Al-Damegh et al., 2005). This information was compiled and averaged to create an initial layered 1D model. The thickness of upper crustal layers was set at 2 km, while lower crustal layers were set to 5 km. It is desirable to use the best events in the dataset to develop the 1D minimum model. These best events were identified as those having more than eight recorded arrivals and an azimuthal separation less than  $180^\circ$ . Approximately 2000 events met the “best data” criteria. To insure that the final 1D minimum model was not dependent on a particular subset of data, several different 500-event subsets were tested. Each subset was iteratively inverted for hypocenter locations and 1D velocity structure. Once no dependence was confirmed, one subset was used to

refine the model using the trial and error process of Kissling et al. (1994). Convergence occurred after about six iterations.

Models that were slightly faster and slower than the *a priori* model were also examined to determine the dependence of the final minimum 1D model on the initial model choice. Initial inversions with the *a priori*, fast, and slow starting models did not converge at depths below ~16 km. This is a result of the limited hypocenter depth distribution and station geometry. Almost all the recorded events had hypocenters at depths less than 16 km, and we are unable to resolve the velocity structure at depths where there are no crossing raypaths. Therefore, velocities below 16 km depth were damped to remain fixed, and with this constraint, all three starting models converged.

Various subsets of the “best data” were used to run different VELEST inversions, and similar results were obtained with each trial. That is, there is no dependence in the resulting 1D minimum model on the initial dataset. The final 1D model is shown in Table 1, and this model was used to relocate the best Harrat Lunayyir events. The 1D model and event relocations (Fig. 4) serve as the starting point for double-difference velocity tomography.

**Figure 4.** Cross-section through the middle of the Harrat Lunayyir events, showing the 1D minimum model and the hypocenter locations from VELEST.

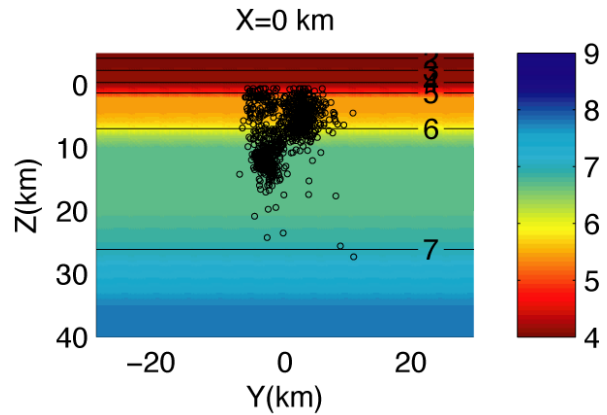


**Table 1. VELEST 1D Model**

| Depth (km) | P-wave Velocity (km/s) |
|------------|------------------------|
| 0.00       | 4.18                   |
| 2.00       | 5.43                   |
| 4.00       | 5.43                   |
| 6.00       | 5.68                   |
| 8.00       | 6.33                   |
| 10.00      | 6.72                   |
| 15.00      | 6.72                   |
| 20.00      | 6.72                   |
| 25.00      | 6.90                   |
| 35.00      | 7.78                   |
| 100.00     | 8.30                   |
| 400.00     | 8.60                   |

## Double-Difference Tomography

The calculation of arrival time to solve for earthquake location depends on earthquake phase picks, initial hypocentral location, and velocity structure, and this leads to a strong coupling between hypocenter and velocity in earthquake location methods (e.g. Kissling et al., 1984; Thurber, 1981; 1992). The *tomoDD* double-difference tomography approach developed by Zhang and Thurber (2003) combines standard local earthquake tomography and double-difference relocation techniques to minimize problems associated with each individual approach. Differential times, especially when calculated using waveform cross-correlation techniques like BCSEIS, help to minimize errors in the velocity model due to pick quality. Simultaneous inversion allows arrival time residuals to become incorporated into the 3D velocity heterogeneity. Overall, this leads to improved accuracy of both absolute and relative earthquake locations as well as the imaging of 3D velocity structure. A hierarchical weighting scheme controls the relative weighting of the absolute and differential time data (Table 2). Weighting parameters are set such that the absolute data first controls the broader-scale velocity structure and then the differential data provides finer resolution near the sources.

Both velocity and station parameter damping affect the resulting velocity model and corresponding resolution estimates (Kissling et al., 2001), and appropriate damping parameters result in a smoothly varying model with minimum data variance (Eberhart-Phillips, 1986). Trade-off curves corresponding to a range of damping (1-500) and smoothing (0.5-5.0) parameters were examined to determine which values minimized the data variance while maintaining low model variance. For P-wave velocity, we selected an initial damping of 190 and smoothing in the x, y, and z directions of 2 for all inversion steps. Slightly reduced damping (170) in later iterations led to reduced RMS misfit. For location-only steps, damping values were chosen such that the condition number (CND), which is defined as the ratio of the largest to smallest eigenvalues, was between 40 and 80, following the work of Waldhauser and Ellsworth (2000). CND has no meaning during the joint inversion steps (Zhang and Thurber, 2003).

Grid spacing was chosen to minimize the variability in the number of raypaths that sample each node in the model (Fig. 5). The catalog data (both absolute and differential times) used in the joint *tomoDD* inversion are optimized by the number of station recordings as well as the connectivity between events, which is established using a nearest neighbor approach (Waldhauser and Ellsworth, 2000). For the Harrat Lunayyir dataset, we required each event to have at least eight neighboring events within a 20 km radius and each event-pair had to have at least eight station recordings. All of the best-constrained events from VELEST met these criteria, and these earthquake hypocenters, along with the associated 1D minimum velocity model, served as the starting point for our 3D inversion. Associated CC differential times were taken from our BCSEIS results. In total, 14,728 absolute catalog times, 202,243 differential catalog times, and 233,720 CC differential times were used in our joint inversion to solve for the P-wave velocity structure.

**Table 2. Hierarchical Weighting Scheme Used with TomoDD**

| NITER | WTCCP | WRCC | WDCC | WTCTDTP | WRCT | WDCT | WTCD | DMP | JNT | THRS |
|-------|-------|------|------|---------|------|------|------|-----|-----|------|
| 1     | 0.01  | -9   | -9   | 0.1     | -9   | -9   | 10   | 190 | 1   | 2    |
| 1     | 0.01  | -9   | -9   | 0.1     | -9   | -9   | 10   | 170 | 0   | 2    |
| 2     | 0.01  | -9   | -9   | 0.1     | 10   | -9   | 10   | 170 | 1   | 2    |
| 2     | 0.01  | -9   | -9   | 0.1     | 10   | -9   | 10   | 180 | 0   | 2    |
| 2     | 0.01  | -9   | -9   | 0.1     | 10   | 10   | 10   | 170 | 1   | 2    |
| 2     | 0.01  | -9   | -9   | 0.1     | 10   | 10   | 10   | 190 | 0   | 2    |
| 2     | 0.01  | -9   | -9   | 1.0     | 10   | 10   | 0.1  | 170 | 1   | 2    |
| 2     | 0.01  | -9   | -9   | 1.0     | 10   | 10   | 0.1  | 230 | 0   | 2    |
| 2     | 0.50  | 10   | -9   | 1.0     | 8    | 8    | 0.1  | 170 | 1   | 3    |
| 2     | 0.50  | 10   | -9   | 1.0     | 8    | 8    | 0.1  | 230 | 0   | 3    |
| 2     | 1.00  | 8    | 8    | 0.5     | 6    | 8    | 0.05 | 170 | 1   | 3    |
| 2     | 1.00  | 8    | 8    | 0.5     | 6    | 8    | 0.05 | 280 | 0   | 3    |
| 2     | 1.00  | 6    | 6    | 0.5     | 6    | 8    | 0.05 | 170 | 1   | 3    |
| 2     | 1.00  | 6    | 6    | 0.5     | 6    | 8    | 0.05 | 280 | 0   | 3    |

NITER: Number of iterations for each weighting parameterization  
 WTCCP: Weight of cross-correlated P-wave differential times  
 WRCC: Factor multiplied by the standard deviation of all cross-correlated times to ID outliers.  
 WDCC: Maximum allowable distance (km) between cross-correlated pairs  
 WTCTDTP: Weight of catalog P-wave differential times  
 WRCT: Factor multiplied by the standard deviation of all catalog times to ID outliers  
 WDCT: Maximum allowable distance (km) between catalog pairs  
 WTCD: Weight of catalog absolute travel-times  
 DMP: Damping applied during nonlinear inversion  
 JNT: 0-event location only; 1-joint event location and velocity inversion  
 THRS: Hit count parameter

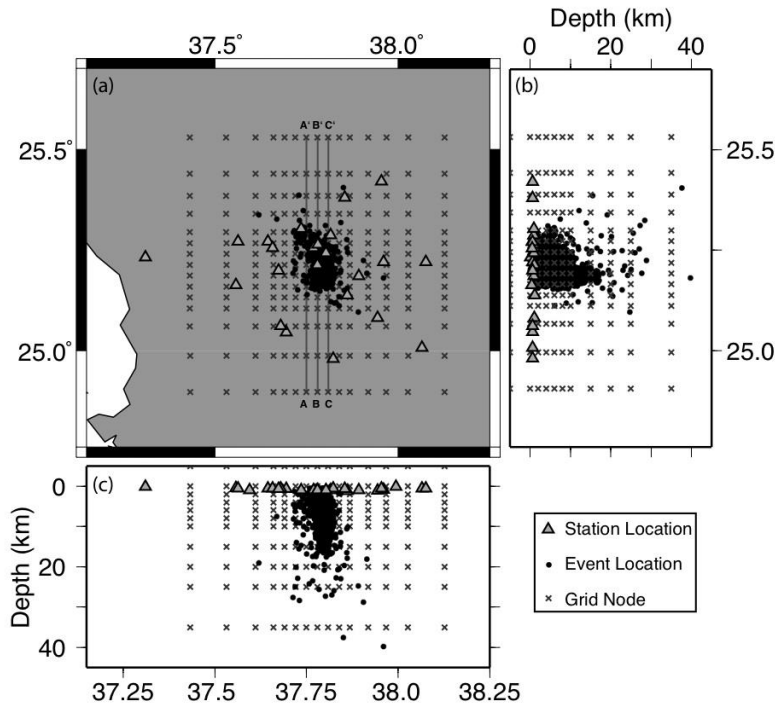


**Figure 5.** Input parameters for tomoDD. (a) Station and event locations are denoted by triangles and dots, respectively. Event locations are those obtained with VELEST and the minimum 1D velocity model. Grid nodes are denoted by gray crosses. Vertical gray lines labeled A-A', B-B', and C-C' denote profile locations shown in Figures 6 and 7. (b and c) Same data shown in cross section.

## Velocity Modeling Results

Our P-wave velocity model is shown in Figure 6. A pronounced fast velocity anomaly is observed beneath Harrat Lunayyir, centered at  $\sim 15$  km depth. From the different cross-sections, it can be seen that this feature is  $\sim 6$  km wide at its thickest point. The fast velocities also extend to somewhat shallower depths ( $\sim 9$  km) to the N-NW, and both of these fast regions coincide with a majority of the local seismicity. These regions of fast velocity are generally surrounded by slower velocities. The best resolved nodes have derivative weighted sum (DWS) values  $\geq 100$  and are located between  $\sim 25.05^\circ\text{N}$  and  $25.35^\circ\text{N}$  latitude and above  $\sim 20$  km depth (Figs. 6-7).

A variety of conditional synthetic tests were examined to assess model resolution, evaluate smearing, and determine expected velocity recovery. Synthetic arrival times were calculated using the same hypocenters, weighting scheme, and ray coverage as the data used in our 3D inversion. Noise was randomly generated between  $\pm 0.05$  s and was added to the synthetic travel times to conservatively estimate uncertainty. The synthetic data was then inverted using the same parameterization as that used for the real data. Figure 8 shows the synthetic velocity model that best mimics the major features observed in our tomographic results. The center of the fast anomaly, as well as the shallower N-NW extension, are well-matched by our model. A conduit-like, fast extension at depth ( $\sim 20$ - $30$  km) may also be present beneath Harrat Lunayyir (Figs. 6 and 8), but since the model has lower DWS values at these depths, this feature is not well resolved.

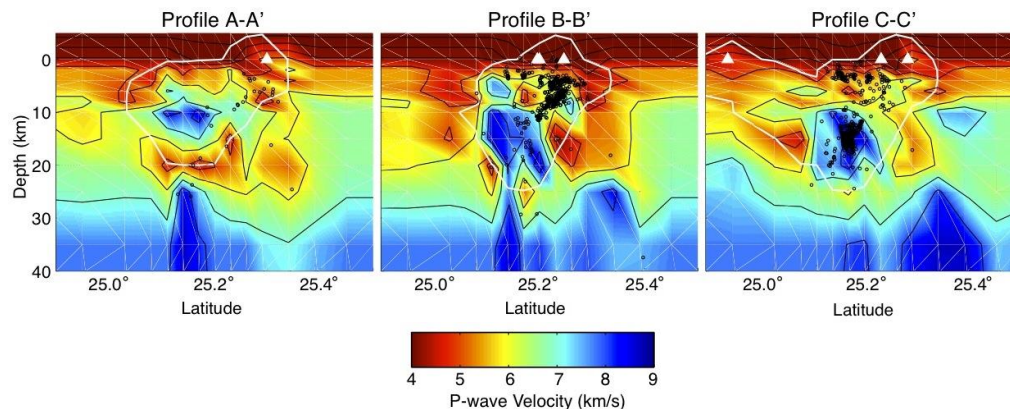


**Figure 6.** South-to-north cross-sections through the 3D P-wave velocity model. Profile locations are shown in Figure 5. Black lines are velocity contours with 1 km/s intervals. Thick white lines encompass nodes with DWS greater than 100; areas outside this line are expected to have reduced or no resolution. White triangles mark station locations and black circles mark event relocations. All depths are referenced to sea level.

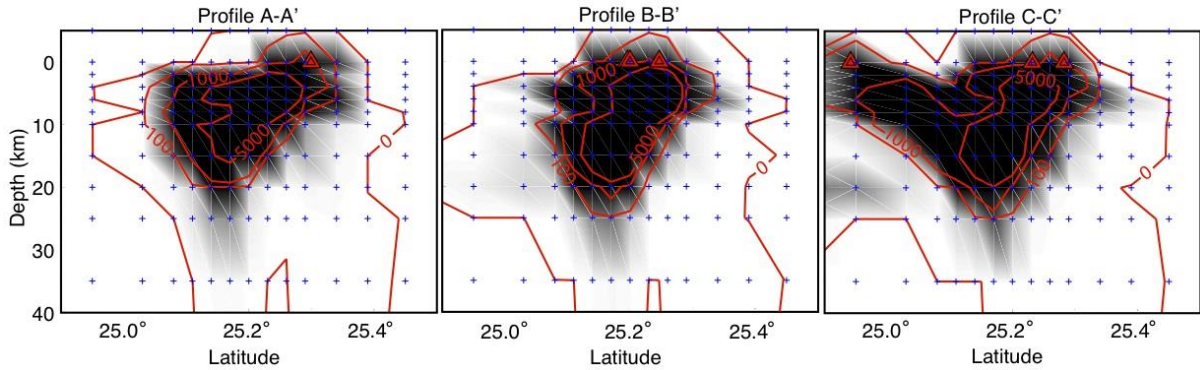
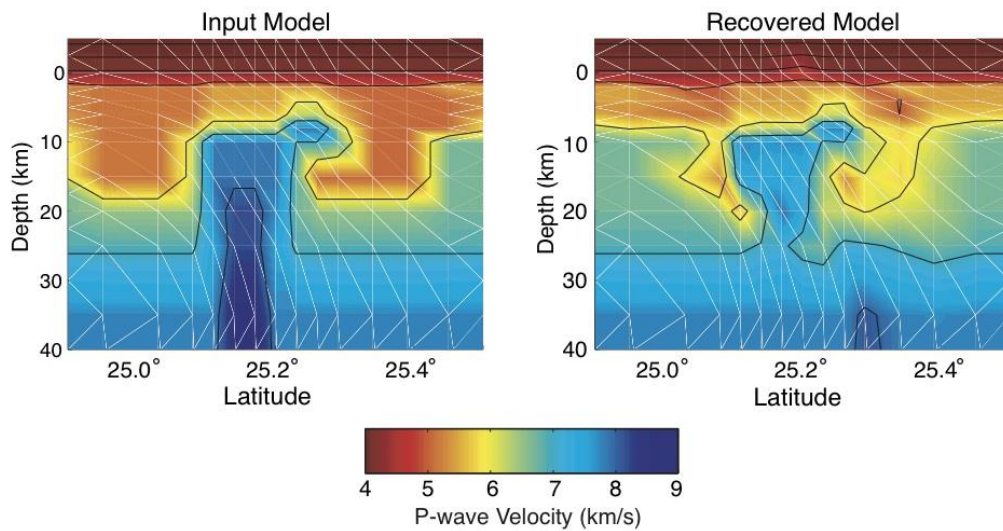


**Figure 7.** DWS contours along cross-sectional profiles. DWS is a weighted measure of the number of data sampling each volume represented by a grid node. Darker shading indicates higher DWS values, and red lines contour values of 0, 100, 1000, and 5000. Blue crosses mark grid nodes and red triangles denote stations along each profile. Given the rapid DWS increase inside the 100 contour, nodes with DWS greater than 100 were considered sufficiently resolved for interpretation.

**Figure 8.** Synthetic velocity models. The input model (left) includes a fast anomaly centered at ~15 km depth, with a shallower extension (~9 km) to the N-NW and additional fast velocities extending to depth. Slow velocity anomalies surround the fast region. The recovered model (right) provides a good match to the major features observed in our tomographic results (Fig. 6).



## Earthquake Relocation Results

Final event locations for the best-constrained events are shown in Figures 6, 9, and 10. In map view, the earthquakes define a NW-SE trend, extending from  $\sim$ N25.27° to N25.23°. The seismicity then appears to be slightly offset to the SW, where the linear trend continues to  $\sim$ N25.20°. The southern-most events form a somewhat broader cluster (Fig. 9). In cross-section, shallow seismicity is concentrated between  $\sim$ 2-8 km depth. However, a distinct dipping trend of seismicity is observed, deepening to the S-SE, and the deepest earthquakes are concentrated at  $\sim$ 15 km depth. As mentioned previously, the earthquakes generally coincide with regions of fast velocity.

*TomodD* does not formally calculate location uncertainties; therefore we employ a bootstrap approach to estimate the associated error. Baer and Hamiel (2010) indicate that the original event locations have uncertainties of 0.5-1.0 km laterally and 0.8-1.5 km in depth. To be conservative, these uncertainty estimates were doubled. Each original earthquake location was randomly perturbed up to  $\pm$ 2 km laterally and  $\pm$ 3 km vertically, and these adjusted event locations were then relocated with our final 3D P-wave velocity model using the same approach outlined previously. This was repeated 100 times for all earthquakes in our dataset, and the average change in location and depth was computed. Based on this bootstrap approximation, our event locations are constrained to within 0.36 km laterally and 0.63 km in depth.

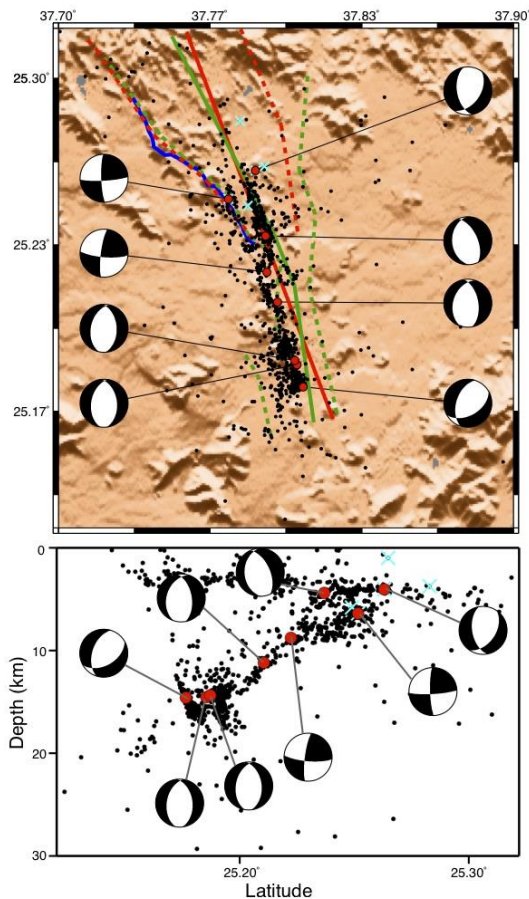


**Figure 9.** Event relocations from *tomodD* (black dots) in both map view (top) and cross-section (bottom). Cyan crosses mark events with magnitudes  $>$  3.5. Red dots mark events (or event clusters) for which focal mechanisms were computed, and these mechanisms are shown along the sides of the plots. On the map view images, red and green lines denote the dyke (solid) and graben-bounding normal faults (dashed) inferred from InSAR modeling from the Pallister *et al.* (2010) and the Baer and Hamiel (2010) studies, respectively. Blue lines denote surface rupture mapped by Pallister *et al.* (2010). The background of each image is a 3 s digital topography map (Farr *et al.*, 2007).

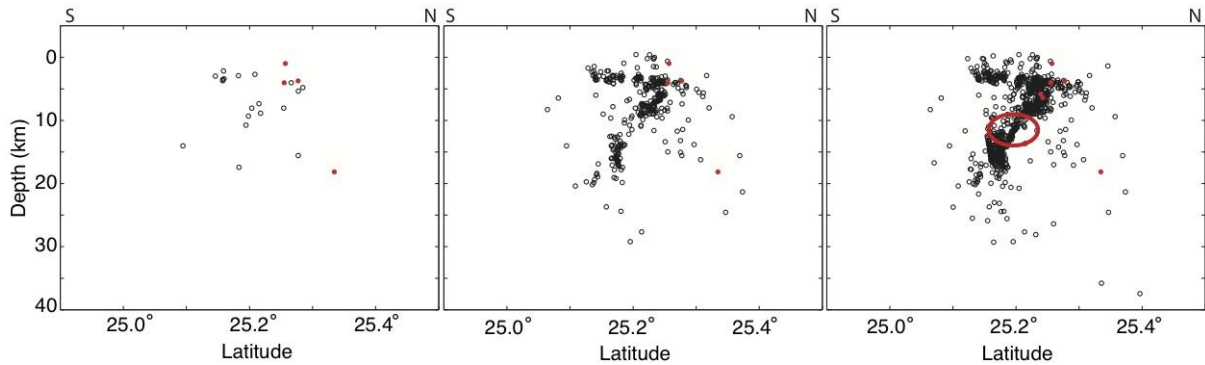


**Figure 10.** South-to-north cross-sections showing earthquake relocations (black circles) as a function of time. Larger magnitude ( $> 3.5$ ) events are highlighted by red dots. [left] Events through May 27, 2009, [center] events through June 28, 2009, [right] events through July 31, 2009. Red ellipse denotes intermediate depth earthquakes.

## Discussion

Modeling of InSAR data following the 2009 seismic swarm at Harrat Lunayyir has indicated that the local deformation is best attributed to the intrusion of a  $\sim 10$  km long, NW-trending dyke, extending from  $\sim 2$  km below the surface down to  $\sim 8$ - $10$  km depth. The associated maximum opening is roughly 2-4 m at  $\sim 5$  km depth, giving the dyke a volume of  $\sim 0.1$  km<sup>3</sup> (Baer and Hamiel, 2010; Pallister et al., 2010). One might expect to see a low velocity anomaly associated with the intrusion, but our velocity model cannot laterally resolve such a narrow (2-4 m) feature. Therefore, the dyke has no velocity signature in our model. Additionally, no significant low velocity anomaly associated with a magma chamber beneath Harrat Lunayyir is observed. It has been suggested that volcanism beneath Harrat Lunayyir is fed by a deep magma source (Camp et al., 1992; Baer and Hamiel, 2010; Zobin et al., 2011). Geochemical analysis has indicated that the majority of volcanic rocks in nearby harrat lava fields were not derived from primary magmas but rather from fractionated liquids that may have resided at moderate crustal depths ( $< 28$  km; Camp et al., 1992). In other words, if a magma body is present, it is likely ponding at depths deeper than those resolved by our model (i.e.  $> 20$  km).

The region surrounding the InSAR-modeled dyke is instead marked by anomalously fast velocities at depth (Fig. 6). It is not uncommon for dykes to repeatedly intrude a given area in the crust (e.g. Dieterich, 1988; Payne et al., 2009; Ebinger et al., 2010; Chadwick et al., 2011), and once solidified at depth, harrat magmas should have significantly higher velocities than the surrounding Precambrian rocks. High velocity features are often found below volcanic regions and rifts and are interpreted as solidified intrusions (e.g. Chiarabba et al., 2000; Keranen et al., 2004; Daly et al., 2008). We suggest that the high velocity body centered beneath Harrat Lunayyir represents a region of solidified magma from previous volcanic episodes, including repeated dyke intrusions that extend to the N-NW. The 2009 dyke intrusion followed this same trend, leading to the observed deformation.

The fast velocity features in our model are generally surrounded by slower velocities (Fig. 6). We interpret this to reflect the true crustal velocities beneath Harrat Lunayyir. That is, where

volcanic rocks do not intrude, the crust is slower than indicated by broader-scale velocity models for the Arabian Shield (*e.g.* Mooney et al., 1985; Mokhtar et al., 1988; Knox et al., 1998; Rodgers et al., 1999; Julià et al., 2003), as represented in our starting model. Crustal velocities increase towards the edges of our model, but the DWS values in these areas are lower and ray coverage is not as complete. The slower crustal P-wave velocities shown in our model are not unreasonable, and in fact compare quite well with global models such as PREM (Dziewonski and Anderson, 1981), IASP (Kennett and Engdahl, 1991), and ak135 (Kennett et al., 1995).

Our earthquake relocations delineate some interesting features throughout the study area as well. Generally, events are deeper in the south and shallower in the north, consistent with preliminary earthquake locations from the SGS (Baer and Hamiel, 2010), and the relocations coincide with fast velocity anomalies imaged in our model (Fig. 6). In map view, the linear trends of seismicity correspond well with the InSAR-modeled dyke orientation (Fig. 9).

To assess any temporal-spatial patterns, we have plotted the earthquake relocations as a function of time (Fig. 10). InSAR modeling suggests that 75% of the deformation and the main period of maximum seismic energy release occurred during May 8-27, 2009 (Pallister et al., 2010; Baer and Hamiel, 2010). Our seismic dataset during these dates is rather limited, but Figure 10 [left] shows that earthquakes occurring during this time were primarily shallow events (~2-8 km) in the northern section of Harrat Lunayyir. Perhaps more interesting is that a majority of all the large magnitude (> 3.5) events in our dataset occurred during this time. 25% of the deformation occurred during May 27 – June 28, with only negligible deformation in July (Pallister et al., 2010; Baer and Hamiel, 2010); however, a considerable number of earthquakes still occurred during this time. Shallow, northern events continued but deep events (~15 km) beneath southern Harrat Lunayyir also occurred. In mid- to late-July, a group of intermediate depth earthquakes developed, connecting the shallow and deep regions of seismicity (Fig. 10).

The deformation and stress fields associated with dyke intrusions are complicated and can lead to a variety of failure mechanisms (*e.g.* Rubin, 1992; Bonafede and Danesi, 1997; Rubin et al., 1998). To better assess the faulting processes associated with shallow, intermediate, and deep earthquakes from the Harrat Lunayyir swarm, focal mechanisms were computed following an approach similar to Hansen et al. (2006). Cross-correlation values from BCSEIS at reference station KSU1 were used to identify clusters of similar events. Since most of our data are small magnitude earthquakes, grouping them into similar families allows first-motion polarity to be more reliably identified. Individual, larger magnitude (> 3.5) events were also examined. Focal mechanisms were computed assuming a double couple source using FOCMEC (Snoke et al., 1984). For clustered events, the polarity observations and an average hypocenter location for each group were used to generate a composite focal mechanism. While there are variations in the fault plane orientations, earthquakes at all depths (shallow, intermediate, and deep) primarily display normal faulting, consistent with tensional opening (Fig. 9). Several strike-slip mechanisms are also observed, which are not uncommon during dike intrusion (Belachew et al., 2012; Shuler and Nettles, 2012), and they indicate dyke-perpendicular opening. One larger magnitude event also displays a thrust mechanism, but it should be noted that the location of this event is not as well constrained as some of the others (Fig. 9).

The imaged velocity structure, the temporal-spatial distribution of the earthquakes, and the corresponding focal mechanisms, in conjunction with InSAR-modeled results, lead to some important interpretations about the 2009 Harrat Lunayyir seismic-volcanic event. During mid- to late-May, the dyke ascended toward the surface following a N-NW trend marked by solidified magmas from previous intrusions. Shallow earthquakes occurred during this time, including most of the largest magnitude events, and these likely reflect brittle failure above and ahead of the intrusion (Belachew et al., 2012; Shuler and Nettles, 2012). From late-May to late-June, the dyke continued to thicken and lengthen, and shallow events beneath northern Harrat Lunayyir continued. Additionally, deeper earthquakes beneath the southern end of the study region also developed. These may reflect responses to the local stress conditions following the intrusion. It is also interesting to note that the shift from shallow to deep events coincides with the southern termination of the wedge-shaped graben that formed during the episode (Fig. 9; Baer and Hamiel, 2010). In mid- to late-July, toward the end of the seismic swarm, earthquakes at an intermediate depth occurred, connecting the shallow and deep regions of seismicity. It is plausible that this “middle” region was stressed by previous, surrounding events and that eventually failure occurred in this area as well.

## **Conclusions**

Using double-difference tomography, we have developed a P-wave velocity model beneath Harrat Lunayyir in northwestern Saudi Arabia. As part of the joint inversion, earthquakes from the 2009 seismic swarm have been more precisely located. Our results are unique since harrat magma systems are rarely imaged, and understanding their velocity structure is important in assessing both local tectonics as well as future seismic and volcanic hazards. Beneath Harrat Lunayyir, fast velocity anomalies have been interpreted as regions marked by repeated volcanic intrusions, oriented NNW-SSE. The crust surrounding the fast intrusions is slower than that suggested by broader-scale models for the Arabian Shield. The largest magnitude earthquakes occurred early in the swarm, concentrated at shallow depths beneath northern Harrat Lunayyir, and these events are associated with the dyke intrusion. Later events include deep earthquakes beneath the southern end of the study area as well as a group of intermediate depth earthquakes that connect the deep and shallow regions of seismicity. These later events likely represent responses to local stress conditions following the intrusion. Our findings are in agreement with previous studies, which modeled surface deformation in Harrat Lunayyir using InSAR data (Baer and Hamiel, 2010; Pallister et al., 2010). Given our observations, coupled with the history of seismic swarms in this region, future volcanic intrusions beneath Harrat Lunayyir seem plausible.

## **Acknowledgements**

We thank the National Plan for Science and Technology, KACST-KSU (09-INF945-02), the Saudi Society for Geosciences, and the SGS for providing the necessary funding as well as the earthquake data that made this project possible. We also thank Sigurjón Jónsson, John Pallister, and Gidi Baer for providing the InSAR-modeled feature coordinates from their respective studies and for several helpful discussions.

## References

- Al-Damegh, K., E. Sandvol, M. Barazangi. Crustal structure of the Arabian plate: New constraints from the analysis of teleseismic receiver functions, *Earth Planet. Sci. Lett.*, 231, 177-196, 2005.
- Baer, G., Y. Hamiel. Form and growth of an embryonic continental rift: InSAR observations and modeling of the 2009 western Arabia rifting episode, *Geophys. J. Int.*, 182, 155-167, 2010.
- Belachew, M., C. Ebinger, D. Coté. Source mechanisms of dike-induced earthquakes in the Dabbahu-Manda Hararo rift segment in Afar, Ethiopia: implications for faulting above dikes, *Geophys. J. Int.*, 192, 907-917, 2012.
- Bonafede, M., S. Danesi. Near-field modifications of stress induced by dyke injection at shallow depth, *Geophys. J. Int.*, 130, 435-448, 1997.
- Camp, V.E., M.J. Roobol, P.R. Hooper. The Arabian continental alkali basalt province: Part II. Evolution of Harrats Khaybar, Ithnayn, and Kura, Kingdom of Saudi Arabia, *Geol. Soc. Am. Bull.*, 103, 363-391, 1992.
- Chadwick, W.W., S. Jónsson, D.J. Geist, M. Poland, D.J. Johnson, S. Batt, K.S. Harpp, A. Ruiz. The May 2005 eruption of Fernandina volcano, Galápagos: The first circumferential dike intrusion observed by GPS and InSAR, *Bull. Volcanol.*, 73, 679-697, 2011.
- Chiarabba, C.A., E. Amato, E. Boschi, F. Barbari. Recent seismicity and tomographic modeling of the Mount Etna plumbing system, *J. Geophys. Res.*, 105(B5), 10,923-10,938, 2000.
- Crotwell, H.P., T.J. Owens. The TauP Toolkit: Flexible Seismic Travel-Time and Raypath Utilities, Version 2.1, University of South Carolina, 1998.
- Daly, E., D. Keir, C.J. Ebinger, G.W. Stuart, I.D. Bastow, A. Ayele. Crustal tomographic imaging of a transitional continental rift: the Ethiopian rift, *Geophys. J. Int.*, 172, 1033-1048, 2008.
- Dieterich, J.H. Growth and persistence of Hawaiian rift zones, *J. Geophys. Res.*, 93, 4258-4270, 1988.
- Du, W., C.H. Thurber, D. Eberhart-Phillips. Earthquake relocation using cross correlation time delay estimates verified with the bispectrum method, *Bull. Seismol. Soc. Am.*, 94, 856-866, 2004.
- Dziewonski, A.M., D.L. Anderson. Preliminary reference Earth model, *Phys. Earth Planet. Int.*, 25, 297-356, 1981.
- Eberhart-Phillips, D. Three-dimensional velocity structure in Northern California Coast Ranges from inversion of local earthquake arrival times, *Bull. Seismol. Soc. Am.*, 76, 1025-1052, 1986.

- Ebinger, C., A. Ayele, D. Keir, J. Rowland, G. Yirgu, T. Wright, M. Belachew, I. Hamling. Length and timescales of rift faulting and magma intrusion: The Afar rifting cycle from 2005-present, *Annu. Rev. Earth Planet. Sci.*, *38*, 439-466, 2010.
- Farr, T.G., P.A. Rosen, E. Caro, R. Crippen, R. Duren, S. Hensley, M. Kobrick, M. Paller, E. Rodriguez, L. Roth, D. Seal, S. Shaffer, J. Shimada, J. Umland, M. Werner, M. Oskin, D. Burbank, D. Alsdorf. The Shuttle Radar Topography Mission, *Rev. Geophys.*, *45*, doi: 10.1029/2005RG000183, 2007.
- Hansen, S.E., S.Y. Schwartz, H.R. DeShon, V. González. Earthquake Relocation and Focal Mechanism Determination Using Waveform Cross Correlation, Nicoya Peninsula, Costa Rica, *Bull. Seism. Soc. Am.*, *96*, 1003-1011, 2006.
- Hansen, S.E., H.R. DeShon, M.M. Moore-Driskell, A.M.S. Al-Amri. Investigating the P wave velocity structure beneath Harrat Lunayyir, northwestern Saudi Arabia, using double-difference tomography and earthquakes from the 2009 seismic swarm, *J. Geophys. Res.*, *118*, 1-13, 2013.
- Julia, J., C.J. Ammon, R.B. Herrmann. Lithospheric structure of the Arabian Shield from the joint inversion of receiver functions and surface-wave group velocities, *Tectonophysics*, *371*, 1-21, 2003.
- Kennett, B.L.N., E.R. Engdahl. Constraints on seismic velocities in the Earth from travel times, *Geophys. J. Int.*, *122*, 108-123, 1995.
- Keranen, K., S.L. Klemperer, R. Gloaguen, the EAGLE Working Group. Three-dimensional seismic imaging of a protoridge axis in the Main Ethiopian rift, *Geology*, *32*, 949-952, 2004.
- Kissling, E., W.L. Ellsworth, R. Cockerham. Three-dimensional structure of the Long Valley Caldera, California, region by geotomography, U.S. Geol. Surv. Open File Rep., 84-939, 188-220, 1984.
- Kissling, E., W.L. Ellsworth, D. Eberhart-Phillips, U. Kradolfer. Initial reference models in local earthquake tomography, *J. Geophys. Res.*, *99*, 19,635-19,646, 1994.
- Kissling, E., S. Husen, F. Haslinger. Model parameterization in seismic tomography: A choice of consequences for the solution quality, *Phys. Earth Planet. Int.*, *123*, 89-101, 2001.
- Knox, R.P., A.A. Nyblade, C.J. Langston. Upper mantle S velocities beneath the Afar and western Saudi Arabia from Rayleigh wave dispersion, *Geophys. Res. Lett.*, *25*, 4233-4236, 1998.
- Michael, A.J. Effects of three-dimensional velocity structure on the seismicity of the 1984 Morgan Hill, California, aftershock sequence, *Bull. Seismol. Soc. Am.*, *78*, 1199-1221, 1988.

- Mokhtar, T.A., R.B. Herrmann, D.R. Russell. Seismic velocity and Q model for the shallow structure of the Arabian Shield from short-period Rayleigh waves, *Geophys.*, *53*, 1379-1387, 1988.
- Mooney, W.D., M.E. Gettings, H.R. Blank, J.H. Healy. Saudi Arabian Seismic-Refraction Profile: A travelttime interpretation of crustal and upper mantle structure, *Tectonophys.*, *111*, 173-246, 1985.
- Pallister, J.S., W.A. McCausland, S. Jonsson, Z. Lu, H.M. Zahran, S. El Hadidy, A. Aburukbah, I.C.F. Stewart, P.R. Lundgren, R.A. White, M.R.H. Moufti. Broad accommodation of rift-related extension recorded by dyke intrusion in Saudi Arabia, *Nature Geosc.*, *3*, doi: 10.1038/NCEO966, 2010.
- Payne, S.J., W.R. Hackett, R.P. Smith. Paleoseismology of Volcanic Environments, in *Paleoseismology*, ed. J.P. McCalpin, 271-314, 2009.
- Rodgers, A.J., W.R. Walter, R.J. Mellors, A.M.S. Al-Amri, Y. Zhang. Lithospheric structure of the Arabian Shield and Platform from complete regional waveform modeling and surface wave group velocities, *Geophys. J. Int.*, *138*, 871-878, 1999.
- Rubin, A.M. Dike-induced faulting and graben subsidence in volcanic rift zones, *J. Geophys. Res.*, *97*, 1839-1858, 1992.
- Rubin, A., D. Gillard, J. Got. A reinterpretation of seismicity associated with the January 1983 dike intrusion at Kilauea volcano, Hawaii, *J. Geophys. Res.*, *103*, 10,003-10,015, 1998.
- Sandvol, E., D. Seber, M. Barazangi, F. Vernon, R. Mellors, A. Al-Amri. Lithospheric seismic velocity discontinuities beneath the Arabian Shield, *Geophys. Res. Lett.*, *25*, 2873-2876, 1998.
- Shuler, A., M. Nettles. Earthquake source parameters for the 2010 western Gulf of Aden rifting episode, *Geophys. J. Int.*, *190*, 1111-1122, 2012.
- Snoke, J.A., J.W. Munsey, A.C. Teague, G.A. Bollinger. A program for focal mechanism determination by combined use of polarity and SV-P amplitude ratio data, *Earthquake Notes*, *55*, 15, 1984.
- Thurber, C.H. Earth structure and earthquake locations in the Coyote Lake area, central California, *PhD thesis*, Massachusetts Institute of Technology, Boston, MA, 339 pp., 1981.
- Thurber, C.H. Hypocenter-velocity structure coupling in local earthquake tomography, *Phys. Earth Planet. Int.*, *7*, 55-62, 1992.
- van der Hilst, R.D., W. Spakman. Importance of the reference model in linearized tomography and images of subduction below the Caribbean plate, *Geophys. Res. Lett.*, *16*, 1093-1096, 1989.

van der Hilst, R.D., R. Engdahl, W. Spakman, G. Nolet. Tomographic imaging of subducted lithosphere below northwest Pacific island arcs, *Nature*, 353, 37-43, 1991.

Waldhauser, F., W.L. Ellsworth. A double-difference earthquake location algorithm: Method and application to the northern Hayward Fault, California, *Bull. Seismol. Soc. Am.*, 90, 1353-1368, 2000.

Wessel, P., W. Smith. New, improved version of the Generic Mapping Tools Released, *Eos Trans., AGU*, 79, 579, 1998.

Zhang, H., C. Thurber, C. Rowe. Automatic P-wave Arrival Detection and Picking with Multiscale Wavelet Analysis for Single-Component Recordings, *Bull. Seismol. Soc. Am.*, 93, 1904-1912, 2003.

Zhang, H., C.H. Thurber. Double-difference tomography: the method and its application to the Hayward Fault, California, *Bull. Seismol. Soc. Am.*, 93, 1875-1889, 2003.

Zobin, V.M., A.M. Al-Amri, M. Fnais. Seismicity associated with active, new-born, and re-awakening basaltic volcanoes: case review and the possible scenarios for the Harrat volcanic provinces, Saudi Arabia, *Arab. J. Geosci.*, 6, 529-541, 2011.